**Key Points:**
- Tropospheric and stratospheric side effects of equatorial solar geoengineering are reduced if nonequatorial injections are applied
- Some residual temperature effects from equatorial injection can be offset with multiple injection locations
- There are still residuals in surface climate and the stratosphere that cannot be offset with four injection locations

**Supporting Information:**
- Supporting Information S1

**Correspondence to:**
B. Kravitz,
bkravitz@iu.edu

# Comparing Surface and Stratospheric Impacts of Geoengineering With Different SO$_2$ Injection Strategies

**Ben Kravitz**[1,2] , **Douglas G. MacMartin**[3] , **Simone Tilmes**[4] , **Jadwiga H. Richter**[5] , **Michael J. Mills**[4] , **Wei Cheng**[3] , **Katherine Dagon**[5] , **Anne S. Glanville**[4] , **Jean-Francois Lamarque**[5] , **Isla R. Simpson**[5] , **Joseph Tribbia**[5] , and **Francis Vitt**[4]

[1]Department of Earth and Atmospheric Sciences, Indiana University, Bloomington, IN, USA, [2]Atmospheric Sciences and Global Change Division, Pacific Northwest National Laboratory, Richland, WA, USA, [3]Mechanical and Aerospace Engineering, Cornell University, Ithaca, NY, USA, [4]Atmospheric Chemistry, Observations, and Modeling Laboratory, National Center for Atmospheric Research, Boulder, CO, USA, [5]Climate and Global Dynamics Laboratory, National Center for Atmospheric Research, Boulder, CO, USA

**Abstract** Geoengineering with stratospheric sulfate aerosols can, to some extent, be designed to achieve different climate objectives. Here we use the state-of-the-art Community Earth System Model, version 1, with the Whole Atmosphere Community Climate Model as its atmospheric component (CESM1(WACCM)), to compare surface climate and stratospheric effects of two geoengineering strategies. In one, SO$_2$ is injected into the tropical lower stratosphere at the equator to keep global mean temperature nearly constant under an RCP8.5 scenario, as has been commonly simulated in previous studies. In another, the Geoengineering Large Ensemble (GLENS), SO$_2$ is injected into the lower stratosphere at four different locations (30°N/S and 15°N/S) to keep global mean temperature, the interhemispheric temperature gradient, and the equator-to-pole temperature gradient nearly unchanged. Both simulations are effective at offsetting changes in global mean temperature and the interhemispheric temperature gradient that result from increased greenhouse gases, but only GLENS fully offsets changes in the equator-to-pole temperature gradient. GLENS results in a more even aerosol distribution, whereas equatorial injection tends to result in an aerosol peak in the tropics. Moreover, GLENS requires less total injection than in the equatorial case due to different spatial distributions of the aerosols. Many other aspects of surface climate changes, including precipitation and sea ice coverage, also show reduced changes in GLENS as compared to equatorial injection. Stratospheric changes, including heating, circulation, and effects on the quasi-biennial oscillation are greatly reduced in GLENS as compared to equatorial injection.

## 1. Introduction

Stratospheric sulfate aerosol geoengineering has been discussed as a potential means of temporarily offsetting the effects of anthropogenic CO$_2$ emissions (e.g., Crutzen, 2006; NRC, 2015). This strategy, one of the most studied methods of solar geoengineering, mimics the cooling resulting from large volcanic eruptions. Numerous climate modeling studies have looked at the impact of stratospheric sulfate aerosol geoengineering on various aspects of the climate system; Caldeira et al. (2013), Irvine et al. (2016), NRC (2015), and Rasch et al. (2008b) provide reviews of the impacts on temperature, the hydrologic cycle, the cryosphere, and stratospheric chemistry, among many other features of the climate response.

Recently, the importance of *design* aspects of solar geoengineering have been receiving increased attention in modeling studies (Kravitz et al., 2016; MacMartin et al., 2016; MacMartin & Kravitz, 2019a). Pertinent to stratospheric sulfate aerosol geoengineering, this perspective takes into account that the climate effects of solar geoengineering will depend on the magnitude (e.g., Niemeier & Timmreck, 2015), latitude (Tilmes et al., 2017; Dai et al., 2018), altitude (Tilmes et al., 2018), and time of year of injection (Kravitz & Robock, 2011). The results may also depend on how the sulfate aerosols are formed, for example, SO$_2$ injection, as is done when large volcanic eruptions occur (Robock, 2000) versus direct condensation of H$_2$SO$_4$ droplets to overcome rapid particle growth and thus reduced geoengineering efficacy and increased stratospheric

heating (Pierce et al., 2010; Vattioni et al., 2019). Subject to limitations imposed by physics, one can design solar geoengineering to meet particular chosen objectives by modifying these different degrees of freedom.

This design perspective is particularly important to consider in the context of latitude of injection. In many previous modeling studies involving stratospheric sulfate aerosol geoengineering, $SO_2$ was injected into the lower stratosphere at the equator, with the idea that the Brewer-Dobson circulation would act to transport the aerosols poleward, thus distributing the aerosols relatively evenly and providing approximately uniform cooling globally (Robock et al., 2008). However, numerous side effects of equatorial stratospheric sulfate aerosol geoengineering have been noted. Simulations with complex representations of aerosol microphysics and stratospheric transport (e.g., Heckendorn et al., 2009; Niemeier et al., 2011; Niemeier & Timmreck, 2015; Tilmes et al., 2017) indicate that equatorial $SO_2$ injection tends to result in a peak in zonal average stratospheric aerosol optical depth (AOD) in the tropics. English et al. (2012) conducted a variety of simulations using different aerosol precursors and different latitudinal extents of injection and found that if injection is centered equatorially, there is still a mass peak near the equator. As such, although global mean temperature increases can be offset by equatorial injection, the surface tends to be overcooled (relative to the baseline of comparison) in the tropics and undercooled at the poles (e.g., Kravitz et al., 2013). Because of differences in land surface area, the Northern Hemisphere tends to be cooled more than the Southern Hemisphere, shifting meridional temperature gradients. Note that $CO_2$ warms the Northern Hemisphere more than the Southern Hemisphere; different models have different sensitivities of the interhemispheric temperature gradient to $CO_2$ versus solar geoengineering (e.g., Kravitz et al., 2016). In addition, simulations with equatorial geoengineering have been associated with notable adverse impacts on column stratospheric ozone (Pitari et al., 2014; Tilmes et al., 2008; Tilmes et al., 2009) and the quasi-biennial oscillation (QBO; Aquila et al., 2014; Richter et al., 2017).

Recently, Tilmes et al. (2017) described a suite of stratospheric sulfate aerosol geoengineering simulations using CESM1(WACCM), a state-of-the-art Earth System Model that includes thorough treatments of stratospheric chemistry and aerosol microphysical growth (Mills et al., 2017). These simulations involved a more comprehensive exploration of the aforementioned design space than has been performed in the past, including stratospheric injection of $SO_2$ at seven different latitudes. As might be expected, injection of $SO_2$ at different latitudes results in different patterns of AOD coverage. Examples include aerosols being relatively confined to one hemisphere for injections poleward of 30° latitude and tropical aerosol coverage without the equatorial peak for simultaneous injection at 15°N and S.

This suite of simulations was performed in preparation for a simulation described by Kravitz et al. (2017) in which a feedback algorithm (MacMartin et al., 2014) was used to independently adjust the annual injection rate of $SO_2$ at four independent locations to achieve three simultaneous global temperature objectives. (This simulation and the objectives are described in more detail in the next section.) In particular, in addition to reducing global mean temperature, the objectives of this strategy were to avoid side effects of regional temperature change, such as different meridional temperature gradients or overcooling of the tropics and undercooling of the poles. Indeed, tropical overcooling and polar undercooling were the original motivations behind moving to a design perspective for geoengineering (Ban-Weiss & Caldeira, 2010; Kravitz et al., 2016). In addition to generally avoiding these regional side effects, Richter et al., 2017 (2017, 2018) found that many of the stratospheric side effects associated with equatorial injection (described previously) were not present in this new simulation, for example, the QBO remains closer to present day than in the RCP8.5 simulation. However, these simulations were not directly compared in the same model with equatorial-only injection. Does this stratospheric aerosol geoengineering strategy have fewer side effects than equatorial injection?

Here we explore this question in more detail by comparing two suites of geoengineering simulations. One involves using equatorial $SO_2$ injection to offset changes in global mean temperature under increased anthropogenic greenhouse gas (GHG) concentrations. The other involves using $SO_2$ injection at four different latitudes (15°N/S and 30°N/S) to offset changes in global mean temperature, the interhemispheric temperature gradient, and the equator-to-pole temperature gradient. We focus on a comparison between the surface climate effects in the two ensembles (section 3), as well as aerosol distribution and mechanisms
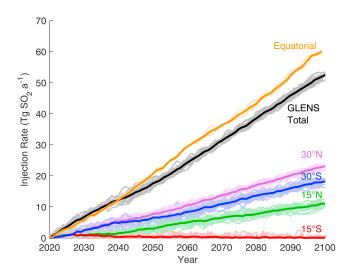
**Figure 1.** Annual injection rates (Tg $SO_2$ $a^{-1}$) for equatorial injection (orange) and Geoengineering Large Ensemble (GLENS, other colors). Individual ensemble members are shown in faint lines, and ensemble averages are shown in thick lines.

of large-scale stratospheric circulation changes (section 4). In doing so, we provide further information regarding the consideration of solar geoengineering as a design problem.

## 2. Simulations and Analysis

The analyses in this study were conducted on three ensembles of simulations, all generated with the 1° horizontal resolution version of CESM1(WACCM) as described by Mills et al. (2017), with the exception of an updated land model, as described by Tilmes et al. (2018). The atmospheric component of this model has 70 vertical layers extending up to 140 km. It is fully coupled to land (CLM4.5; Oleson et al., 2013), ocean (POP2; Danabasoglu et al., 2012), and cryospheric (CICE4; Hunke & Lipscomb, 2008) components. Aerosol microphysics are handled via the three-bin Modal Aerosol Model (MAM3; Liu et al., 2012). The coupled model system validates well against observed AOD from the 1991 eruption of Mount Pinatubo. Mills et al. (2017) provide further details regarding the model development, components, and validation procedure.

The first ensemble serves as a baseline for comparison against the geoengineering simulations. A 20-member ensemble of RCP8.5 simulations (van Vuuren et al., 2011) was conducted over the period 2010–2030; the average over this period is referred to as *baseline* conditions. Three of those ensemble members were extended out past 2095. In the second ensemble, hereafter called the Geoengineering Large Ensemble (GLENS; Tilmes et al., 2018), $SO_2$ was injected at four independent locations: 30°N, 15°N, 15°S, and 30°S (each into a single grid box at 180°E, at the model level ≈5 km above the annual mean tropopause). These locations were chosen because MacMartin et al. (2017) found that they are sufficient to meet the chosen objectives of GLENS. The amount of injection at each location was adjusted independently every year by employing feedback on the previous climate state, as described by Kravitz et al. (2017). The feedback algorithm involves evaluating the model state after every year of simulation, specifically in terms of how far the state is from the chosen objectives. Then the injection amount at each of the four locations is adjusted independently to better meet the objectives. For a more thorough description of feedback as applied to solar geoengineering, please refer to MacMartin et al. (2014) and Kravitz et al. (2016). The objectives of this feedback algorithm are, starting in 2020, to maintain global mean surface air temperature ($T_0$), the interhemispheric surface air temperature gradient ($T_1$), and the equator-to-pole surface air temperature gradient ($T_2$) at baseline (2010–2030 average) values against a background of RCP8.5 over the period 2020–2099. More formally, these quantities are defined as

$$
\begin{aligned}
T_0 &= \frac{1}{A} \int_{-\pi/2}^{\pi/2} T(\psi)\,dA \\
T_1 &= \frac{1}{A} \int_{-\pi/2}^{\pi/2} T(\psi)\sin\psi\,dA \\
T_2 &= \frac{1}{A} \int_{-\pi/2}^{\pi/2} T(\psi)\frac{1}{2}(3\sin^2\psi - 1)\,dA
\end{aligned}
\tag{1}
$$

where $T(\psi)$ is zonal mean temperature at latitude $\psi$, $A = \int_{-\pi/2}^{\pi/2} \cos(\psi)\,d\psi$ denotes area, and $dA$ is an area weighting. GLENS involves 20 ensemble members.

In the third ensemble, referred to as equatorial injection (or abbreviated GEQ in some of the figure titles), $SO_2$ was injected only at the equator (in a single grid box, also at 180°E, also 5 km above the annual mean tropopause) to maintain $T_0$ at its baseline (2010–2030 average) value against the same RCP8.5 background as GLENS over the period 2020–2099. This was again accomplished by employing feedback, adjusting the rate of $SO_2$ injection every year. Three ensemble members of this simulation were performed.

In some plots, statistical significance is shown. Because the two sets of simulations being compared have different ensemble sizes and potentially different variances, statistical significance is calculated using Welch's $t$ test. Stippling is shown where results are *not* statistically significant at the 95% confidence level.
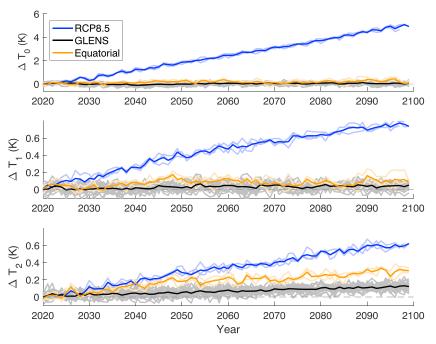
**Figure 2.** Change in annual mean (top) $T_0$, (middle) $T_1$, and (bottom) $T_2$ (equation (1); K) from the baseline period (Representative Concentration Pathway 8.5, RCP8.5, 2010–2030 average) for the RCP8.5 (blue), Geoengineering Large Ensemble (GLENS, black), and equatorial (orange) ensembles. Faint lines indicate individual ensemble members, and thick lines indicate ensemble means.

## 3. Surface Climate Effects

As is seen in Figure 1, the GEQ strategy requires more total $SO_2$ injection than GLENS to achieve the same $T_0$ objective, suggesting a lower efficiency of global average cooling per unit injection. This is in contrast to previous assumptions that tropical injection would be the most efficient because large-scale atmospheric circulation would transport the aerosols to achieve roughly globally uniform coverage (Budyko, 1977; Robock et al., 2008). (We revisit the reasons for this in the subsequent section, specifically surrounding the discussion of particle size.) In GLENS, most of the injection occurs at 30°N and 30°S, with a lesser amount at 15°N. Hardly any injection occurs at 15°S. This results in excellent success in maintaining $T_0$ at baseline levels (Figure 2). $T_1$ has a slight positive bias, but the ensemble mean is still within the ensemble spread of the reference period (Tilmes et al., 2018). GLENS shows some bias in $T_2$ due to saturation in meeting $T_0$ and $T_1$ (MacMartin et al., 2019): meeting $T_2$ while also meeting $T_0$ and $T_1$ would have called for negative $SO_2$ injection at 15°S, which is impossible. Therefore, there was too much tropical cooling relative to high latitudes, which manifests as a positive $T_2$ bias that the feedback algorithm cannot fully correct. In the GEQ ensemble, both $T_0$ and $T_1$ have similar performance to GLENS. In this model, roughly uniformly distributed $CO_2$ (which is the dominant forcing in RCP8.5, although other forcings, such as tropospheric aerosols, are hemispherically asymmetric) warms the Northern Hemisphere more than the Southern Hemisphere and the roughly hemispherically symmetric aerosol distribution from GEQ cools the Northern Hemisphere more than the Southern Hemisphere, resulting in effectively meeting the $T_1$ goal as long as $T_0$ is met, without explicitly specifying $T_1$ as a goal. The major difference between the ensembles is $T_2$: although GEQ partially offsets the change in $T_2$, there is some residual overcooling of the tropics and undercooling of the poles, and only specifically targeting the equator-to-pole temperature gradient, as in GLENS, is effective at further reducing $T_2$ changes.

Niemeier and Timmreck (2015) calculated metrics of forcing efficiency, defined as the instantaneous radiative forcing due to the aerosols (calculated from a double radiation call) per annual injection rate, plotted as a function of the injection rate. Supporting information Figure S1 shows similar plots for both GLENS and GEQ from this study. The magnitude of instantaneous radiative forcing can be artificially high under scenarios of strong heating near the tropopause (Hansen et al., 2005). As such, we can conclude that our GEQ results are qualitatively similar to those of Niemeier and Timmreck (2015): after an initial transient
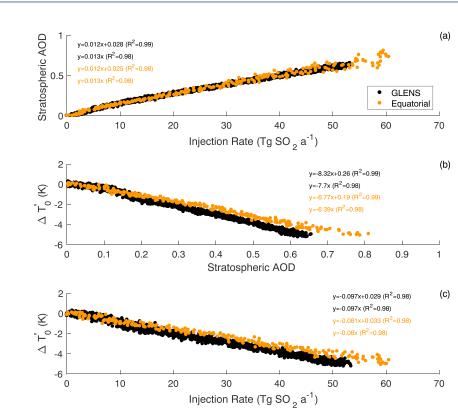
**Figure 3.** Scatter plots of (a) global, annual mean stratospheric AOD; (b) global, annual mean temperature change as compared to the RCP8.5 ensemble ($\Delta T'_0$; K); and (c) annual injection rate for GLENS (black) and equatorial injection (orange). Text in each panel gives the equations for ordinary least squares regression through the points, both unconstrained and constrained to go through the origin, representing different time scales of system response (long-term and initial transient, respectively). GLENS = Geoengineering Large Ensemble; AOD = aerosol optical depth.

period, total forcing efficiency reduces with injection rate, but longwave efficiency does not change appreciably. However, because different simulations have different amounts of stratospheric heating (section 4 below), they will have different biases in their radiative forcing estimates. As such, this metric is limited for comparisons across simulations. Instead, we focus on comparisons of stratospheric AOD, which does not necessarily have the same relationship with injection rate as does radiative forcing (Kleinschmitt et al., 2018). The relationship between injection rate and stratospheric AOD is consistent between GLENS and GEQ (Figure 3a); this will be revisited in the final section. Although there are transient responses toward the beginning of the simulation, when the stratospheric aerosol burden is ramping up, there is no evidence of strong nonlinearity in the majority of the simulations. As a separate metric of efficiency, we calculate the slope of the regression line between injection rate or stratospheric AOD over 2020–2099 against $\Delta T'_0$, where $\Delta T'_0$ is the global mean temperature difference between the geoengineered ensemble and the RCP8.5 ensemble. For both injection rate and stratospheric AOD (Figures 3 b and c), there is an "efficiency penalty" of 19% for GEQ as compared to GLENS.

Figure 4 shows a monthly time series of zonal mean stratospheric AOD for the GLENS ensemble and GEQ cases. Consistent with previous studies (e.g., Niemeier et al., 2011; Pitari et al., 2014; Tilmes et al., 2017), the GEQ case results in a peak in AOD near the equator, lesser peaks in the midlatitudes, and relative gaps in the subtropics. Conversely, GLENS shows peaks in the midlatitudes and a relative gap in the tropics. There is a notable seasonal cycle in AOD at all latitudes. Peak AOD (over all latitudes and months) reaches approximately 1 in both ensembles by the end of the century.

Disaggregating these results into zonal mean surface air temperature (Figure 5), the RCP8.5 simulation looks as expected: warming everywhere due to increased GHG concentrations, with greater warming at the poles (especially the Arctic) due to feedbacks and transport processes associated with polar amplification (Holland & Bitz, 2003). Comparing GLENS and GEQ, it becomes immediately clear that GLENS is effective at offsetting the known feature of "overcooling" in the tropics and "undercooling" at higher latitudes that is
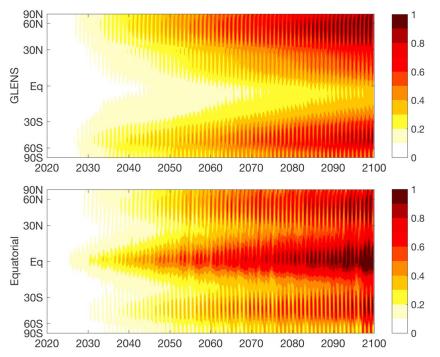
**Figure 4.** Zonal mean stratospheric aerosol optical depth for the ensemble mean of GLENS (top) and equatorial injection (bottom). All values are monthly means. GLENS = Geoengineering Large Ensemble.

associated with idealized solar reduction (e.g., Govindasamy & Caldeira, 2000; Kravitz et al., 2013) or more realistic stratospheric sulfate aerosol (e.g., Tilmes et al., 2017) representations of stratospheric sulfate aerosol geoengineering using GEQ of sulfate aerosol precursors. We calculate an area-weighted root-mean-square error (RMSE) metric via

$$\text{RMSE}_A = \sqrt{\frac{\sum \left(T - T_\text{base}\right)^2 dA}{\sum dA}} \tag{2}$$

where $T$ is the temperature in any grid cell averaged over 2075–2095 (ensemble member average), $T_\text{base}$ is the temperature in the baseline (2010–2030 average, ensemble average) in that grid cell, $dA$ is the area of that grid cell, and summation is over all grid cells. $\text{RMSE}_A$ for GLENS is 0.51, 0.56, and 0.76 K for annual mean, June to August (JJA) average, and December to February (DJF) average, respectively. For GEQ, the values are 0.82, 0.87, and 1.11 K, respectively. For context, RCP8.5 values are 4.49, 4.47, and 5.18, respectively. Even though $T_0$, $T_1$, and $T_2$ may be controlled on average (Figure 5c), there can still be significant regional temperature changes, albeit reduced changes in GLENS as compared to GEQ (Figure 6 and supporting information Figure S2; figures in the supporting information show a 2045–2065 average). Both ensembles show Arctic cooling with respect to RCP8.5, more so in GLENS, although the area covered by those latitudes is too small to substantially affect the feedback algorithm behavior (not shown).

The residual warming at midlatitudes in both ensembles resembles a classic winter warming signal (e.g., Driscoll et al., 2012; Robock & Mao, 1992), although the warming in GLENS is more extensive than is typically found after volcanic eruptions (Wunderlich & Mitchell, 2017). The midlatitude warming pattern appears to be stronger in the equatorial run than in GLENS, although it is difficult to disaggregate this feature from the differences in $T_2$ between the ensembles. A further exploration of some potential dynamical changes is undertaken in the next section, although it is an active area of research to understand dynamical effects from geoengineering versus volcanic eruptions, and the results are likely to be model dependent (H. Schmidt, personal communication, March 28, 2019). The right column of Figure 6 indicates that, compared to GLENS, the GEQ ensemble has more tropical cooling and residual warming at other latitudes, consistent with the added objectives of $T_1$ and $T_2$ in GLENS. Both GEQ and GLENS show features of high-latitude cooling during summer. The temperature objectives of the feedback algorithm are defined in the annual mean.
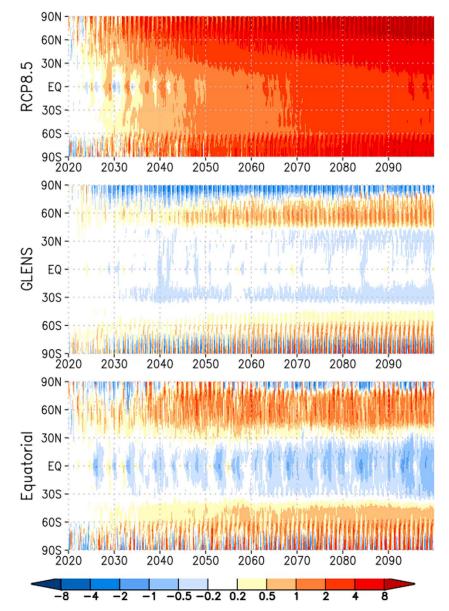
**Figure 5.** Zonal mean surface air temperature change (K) from the baseline period climatology (RCP8.5, average seasonal cycle over 2010–2030) for the ensemble means of RCP8.5 (top), GLENS (middle), and equatorial injection (bottom). All values are monthly means. GLENS = Geoengineering Large Ensemble. RCP = Representative Concentration Pathway.

Therefore, if there are indeed dynamical effects leading to a winter warming pattern as is seen after volcanic eruptions, then meeting the goals requires injection of an amount that will overcool in the summer.

As an additional metric of change, Figure 7 shows changes in atmospheric, oceanic, and total meridional heat flux as a function of latitude, calculated using the method of Wunsch (2005), whereby net TOA and surface radiative fluxes are integrated from the south pole to the north pole. Positive values indicate northward transport. The RCP8.5 simulations result in substantially reduced atmospheric poleward heat flux, which is compensated by increased oceanic flux, resulting in little net annual change. GLENS and the GEQ ensembles have little change in either atmospheric or oceanic fluxes (on an annual average), indicating the effectiveness of these particular deployments of solar geoengineering in offsetting changes in aggregate heat fluxes caused by anthropogenic GHGs. However, RCP8.5 and both geoengineering ensembles show some seasonal change in meridional heat flux. RCP8.5 shows the largest changes: In the boreal summer, there is anomalous southward transport by the atmosphere and anomalous northward transport by the ocean; in the
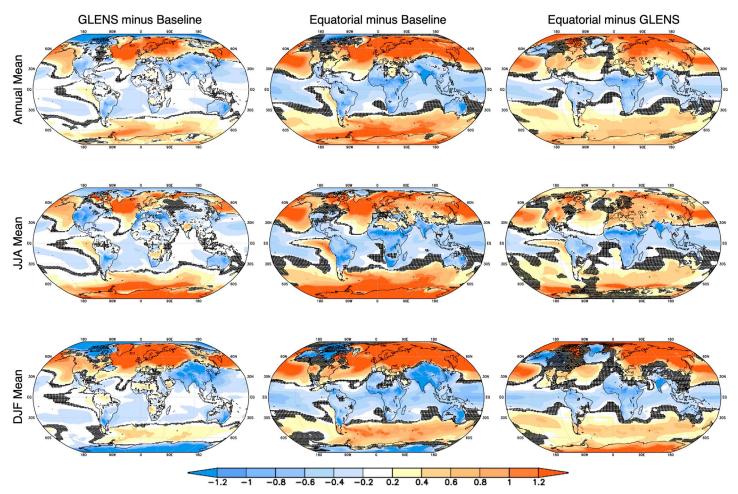
**Figure 6.** Maps of surface temperature change (K) for GLENS (left column), Equatorial (middle column) and the difference Equatorial-GLENS (right column) where change refers to the mean over the period 2075–2095 minus the baseline. Stippling indicates regions that are not statistically significant at the 95% confidence level as calculated using Welch's *t* test. GLENS = Geoengineering Large Ensemble; JJA = June to August; DJF = December to February.

boreal winter, the opposite pattern occurs. In summer and winter, both GLENS and the GEQ simulations show reduced northward meridional heat flux in the atmosphere near the North Pole, which is compensated by the ocean. Hwang and Frierson (2010) found that the bulk of atmospheric meridional heat transport is due to moisture flux, so this is a potential indication of less moisture transport into the Arctic, consistent with the high-latitude cooling discussed earlier. While all of these findings represent a consistent picture, finding a causal relationship will require additional investigation that is beyond the scope of this study.

Figure 8 shows changes in minimum and maximum sea ice extent in both the Northern and Southern Hemispheres. These results largely parallel the previous discussions of high-latitude temperature. Under RCP8.5, due to warming and polar amplification of that warming, sea ice undergoes a precipitous decline. Conversely, both geoengineering simulations show promise in partially restoring sea ice, particularly GLENS in the Arctic, consistent with the sustained cooler temperatures seen in Figures 5 and 6. September sea ice extent increases despite positive $T_2$ values, consistent with the previously discussed temperature changes. This also indicates that large-scale average metrics of performance may not capture important local features of change.

Figure 9 (also, see supporting information Figure S3) shows that none of the geoengineering ensembles offsets all precipitation changes. However, the residual changes in the GEQ ($RMSE_A = 0.41$ mm/day) are greater (as compared to the baseline) than the changes in GLENS ($RMSE_A = 0.25$ mm/day). For reference, in RCP8.5, $RMSE_A = 0.56$ mm/day. Many of the starkest differences between the two ensembles are in the tropics, specifically that GEQ results in tropical drying, consistent with overcooling of the tropics. Because the two ensembles show similar performance in offsetting changes in $T_1$, it is difficult to determine whether
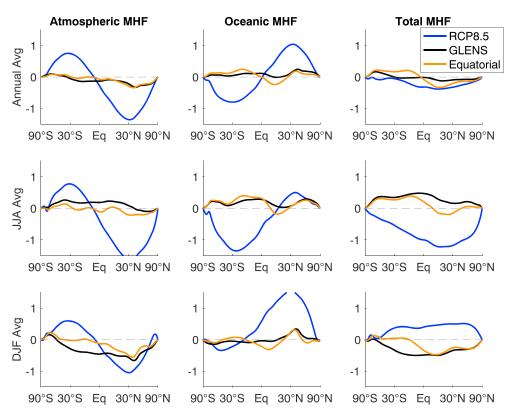
**Figure 7.** Change in ensemble average meridional heat flux (MHF; PW) for RCP8.5 (blue), GLENS (black), and equatorial injection (orange). Values are calculated using the methodology of Wunsch (2005). GLENS = Geoengineering Large Ensemble; RCP = Representative Concentration Pathway.

preventing changes in $T_1$ also prevents shifts in the intertropical convergence zone (ITCZ). Figure S4 shows that both GLENS and GEQ have little change in the latitude of the precipitation centroid, which is a metric of ITCZ position. Frierson and Hwang (2012) argue that shifts in the ITCZ are tied to meridional heat flux changes that may not be reflected in temperature gradient shifts ($T_1$); the potential for devising a feedback algorithm that would target these meridional heat flux changes instead of temperature changes is left to future work. (We note that one could also directly target precipitation as an objective of a feedback algorithm, as was attempted by MacMartin et al. (2014) and Kravitz et al. (2016). However, precipitation is a very noisy field, so there are advantages to targeting objectives like $T_1$, which are arguably less noisy.) In addition, geoengineering can cause dynamical changes (discussed in the following section) that in turn have effects on precipitation. At this point, it is difficult to make conclusions as to what is driving different precipitation changes in the two ensembles or whether those changes are robust. However, we can make the broad conclusion that has been made in numerous other studies (e.g., Bala et al., 2008): carbon dioxide increases (as under RCP8.5), accelerate the hydrological cycle, and global-scale geoengineering offsets that acceleration.

## 4. Stratospheric Changes

As was discussed in the previous section, several features of the climatic response are hypothesized to be related to changes in dynamics, potentially influenced by the stratosphere. Most analyses in this section involve a comparison of years 2075–2095 as compared to the baseline (RCP8.5, 2010–2030 average) for both GLENS and the GEQ ensembles.

Figure 10 illustrates changes in zonally averaged sulfate ($SO_4$) aerosol mass burden. $SO_4$ mass tends to have maxima near the injection locations and lower values away from the injection sites due to transport (Figure 1), augmenting background values by over 3 orders of magnitude. Figure S5 indicates that the increase in $SO_4$ mass burden scales with the increase in $SO_2$ injection rate. The aerosols tend to spread more meridionally in GLENS than under GEQ, with peak values in GLENS being approximately half of the peak values in the GEQ ensemble. These results are consistent with the findings of Tilmes et al. (2017). In
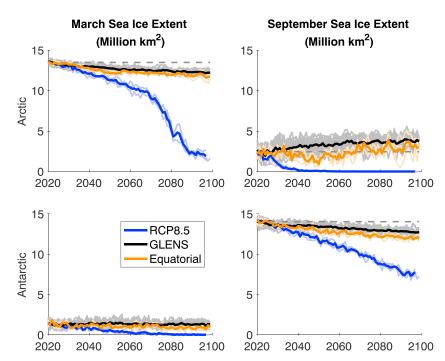
**Figure 8.** (left column) March and (right column) September sea ice extent (millions of square kilometers) for RCP8.5 (blue), GLENS (black), and equatorial injection (orange). For calculations in this figure, Arctic contains all grid boxes north of 45°N, and Antarctic contains all grid boxes south of 45°S. Faint lines depict individual ensemble members, and solid lines depict ensemble averages. RCP = Representative Concentration Pathway; GLENS = Geoengineering Large Ensemble.

both geoengineering ensembles, tropospheric $SO_4$ mass burden increases at all latitudes, consistent with increased deposition (Kravitz et al., 2009; Visioni et al., 2018). Even though the injection heights are similar in both ensembles, the vertical extent of the aerosols is much greater in the GEQ ensemble than in GLENS. Equatorial aerosols are more likely to be transported upward by the upwelling branch of the Brewer-Dobson circulation (Plumb, 2002), although (as discussed shortly) there may be more contribution from self-lofting due to aerosol heating in the equatorial case.

Figures 11 and S6 provide zonally averaged calculations of modeled aerosol effective radius. When aerosol effective radius is averaged spatially, it is important to weight the average by some measure of where the aerosols are, as a straightforward mean will be dominated by large radii in places where there may be few aerosols. An effective strategy is to weight the average by any of the three moments of the size distribution: number density, surface area density, or mass/volume density. For the calculations presented in this study, we choose to weight by surface area density (SAD). This is mathematically equivalent to
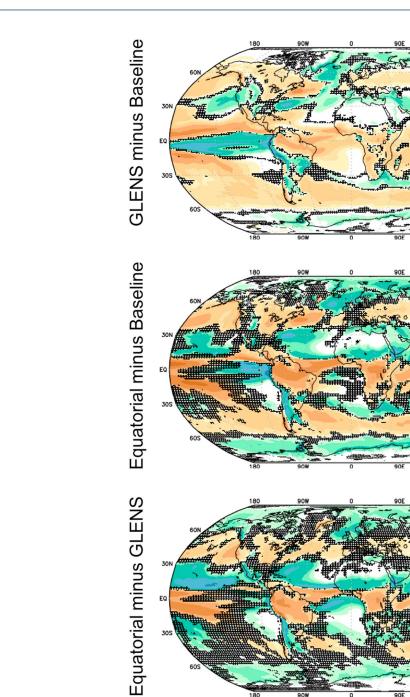
$$\overline{r_{\text{eff}}}(\phi, z) = \frac{\sum_{\lambda} \left[ r_{\text{eff}}(\lambda, \phi, z) \cdot \text{SAD}(\lambda, \phi, z) \right]}{\sum_{\lambda} \text{SAD}(\lambda, \phi, z)} \tag{3}$$

where $\lambda$ indicates longitude, $\phi$ indicates latitude, $z$ indicates altitude, and an overline indicates the zonal average (average over all longitudes).
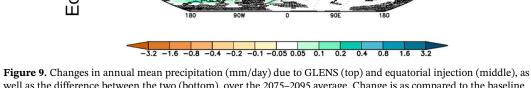
Aerosol effective radius is useful for understanding the increased vertical extent of the aerosols in Figure 10, which could be due to various dynamical interactions associated with heating of the aerosols. In GLENS, aerosol effective radius reaches peak tropical values of ≈0.7 μm, an increase from the baseline and RCP8.5, which each has peak values of ≈0.2 μm. Conversely, aerosol effective radius under GEQ exceeds 1 μm, even as early as the 2045–2065 average period (Figure S6). The meridional distribution of aerosol effective radius has a tropical peak (i.e., the area with maximum concentration) with generally lower values poleward, although this peak is far more pronounced under GEQ.

The patterns of stratospheric temperature change in the two ensembles (Figures 12 and S7) are consistent with the different $SO_4$ mass burdens and effective radii, as well as the radiative effects of increased $CO_2$.

**Figure 9.** Changes in annual mean precipitation (mm/day) due to GLENS (top) and equatorial injection (middle), as well as the difference between the two (bottom), over the 2075–2095 average. Change is as compared to the baseline (RCP8.5, 2010–2030 average). Stippling indicates regions that are not statistically significant at the 95% confidence level as calculated using Welch's *t* test. GLENS = Geoengineering Large Ensemble.

Stratospheric heating is present in both geoengineering ensembles, but GEQ results in approximately 60% more heating than in GLENS. The latitudinal extent of the heating is similar in both ensembles. Most of the heating is below the peak mass mixing ratio but above the tropopause (refer to Richter et al., 2017; Richter et al., 2018, for a more detailed description of the mechanisms governing the location of this heating). Both geoengineering ensembles show slight tropical tropospheric cooling, consistent with reduced insolation,

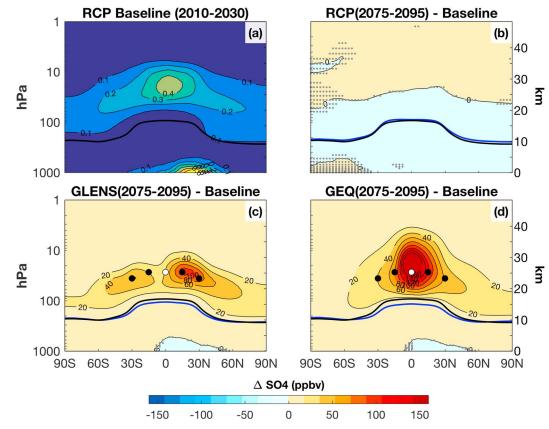**Figure 10.** (a) Baseline (RCP8.5 averaged over years 2010–2030) zonal mean $SO_4$ mass burden ($ppb_v$); (b) change from the baseline for the RCP8.5 ensemble mean, averaged over the period 2075–2095; (c) change from the baseline for the ensemble average of GLENS; and (d) change from the baseline for the equatorial injection ensemble average. Hatching indicates that differences are not statistically significant at the 95% confidence level. The four black circles indicate the four $SO_2$ injection locations in GLENS, and the white circle indicates injection location under equatorial injection. The black solid line indicates the tropopause in the baseline, and the blue solid line indicates the tropopause in the perturbed experiment. Panel (a) has a different color scheme and contouring from the other panels, and the color bar does not apply to panel (a). RCP = Representative Concentration Pathway; GLENS = Geoengineering Large Ensemble; GEQ = equatorial injection.

increased tropospheric stability, and hence less column water vapor (Figures 13 and S7; Bala et al., 2008). Both ensembles also show upper stratospheric cooling of generally comparable magnitude to RCP8.5, which is a known signal of increased GHGs (Manabe & Wetherald, 1975).

Warming of the tropopause by the aerosols allows more water vapor into the stratosphere, as has been observed after large volcanic eruptions (e.g., Figure 13 and Supplemental Figure 8 ; Oman & Waugh, 2008). Water vapor increases in most of the lower stratosphere by 2–4 $ppm_v$ in GLENS and by 4–7 $ppm_v$ in GEQ, compared to the baseline of 3–5 $ppm_v$. Under GEQ, the stratospheric heating tends to be amplified in the tropics, accelerating the transport of water vapor into the stratosphere and resulting in approximately a doubling of the background stratospheric water vapor values, as compared to an ≈50% increase over background values in GLENS.

The increase in stratospheric water vapor concentration is less in both geoengineering ensembles at the poles between 20 and 30 km in altitude as compared to other latitudes, especially at the South Pole. This feature sets up relatively early in the simulations (Figure S8), and the Antarctic feature is also seen in the RCP8.5 simulations. All of these dehydration features are poleward of accelerated zonal wind (Figures 14 and S9), indicating a strengthening of the polar jets. These jets in turn can establish a transport barrier, preventing accumulation of water vapor at high latitudes. Consistent with thermal wind balance, the strengthened stratospheric westerlies are accompanied by cooling in the polar lower stratosphere, as is seen in Figures 12 and S7. Due to a lack of appreciable change in polar stratospheric ozone concentration (Figure S10), the
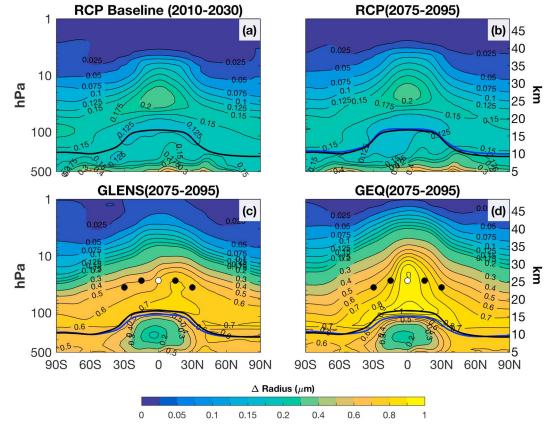
**Figure 11.** Sulfate aerosol effective radius (μm) for (a) Baseline (RCP8.5 averaged over years 2010–2030); (b) RCP8.5 (2075–2095 average); (c) GLENS (2075–2095); and (d) Equatorial injection (2075–2095). Hatching indicates that differences are not statistically significant at the 95% confidence level. The four black circles indicate the four SO$_2$ injection locations in GLENS, and the white circle indicates injection location under equatorial injection. The black solid line indicates the tropopause in the baseline, and the blue solid line indicates the tropopause in the perturbed experiment. RCP = Representative Concentration Pathway; GLENS = Geoengineering Large Ensemble; GEQ = equatorial injection.

explanatory mechanism for polar stratospheric water vapor changes is likely not chemical. (Note that such ozone changes are likely small because by the mid-21st century, stratospheric CFC conditions are assumed to be low in RCP8.5. As such, catalytic destruction of ozone mediated by introducing aerosol surfaces into the stratosphere, as is discussed by Tilmes et al. (2008), is much less of an issue for our simulations.) Zonal wind changes in the GEQ ensemble are twice that of GLENS, helping to explain why the relative decrease in polar water vapor in the equatorial ensemble is more pronounced than in GLENS.

Stratospheric water vapor changes have potential dynamic drivers, which are consistent with the large-scale dynamical changes that induce winter warming seen after large volcanic eruptions. (See Driscoll et al. (2012) for a thorough explanation and a complete list of references.) Tropical stratospheric warming drives increased zonal wind speeds through the thermal wind relationship (Figures 14 and S9); this also explains why changes in zonal wind are larger in GEQ than in GLENS. This in turn drives a more positive phase of the Arctic Oscillation, which drives anomalous advection of relatively warm ocean air over land in the mid-latitudes (e.g., Driscoll et al., 2012). However, as stated previously, some features of residual warming seen in GLENS are not consistent with "classic" winter warming, leading us to conclude that dynamical changes may not be wholly responsible for the results seen here. Further work is warranted to untangle and attribute the residual warming.

In both geoengineering simulations, lower stratospheric zonal wind decelerates around 30°N and 30°S, a reversal of the global warming pattern in RCP8.5 (Richter et al., 2018). In the equatorial simulation, this decrease spreads to the tropics, consistent with a change of the QBO (Figure 15) to a persistent Westerly phase. (See Niemeier & Schmidt, 2017, for a more detailed discussion of the mechanisms for these changes.)
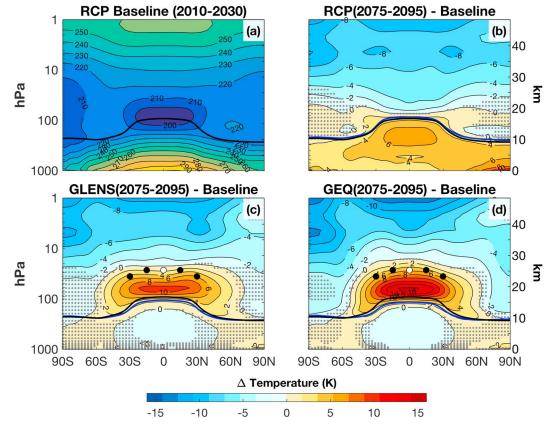
**Figure 12.** As in Figure 10 but for temperature (K).

In GLENS, the tropical zonal wind centered around 25 km in altitude also decreases (Figure 14), unlike under GEQ. As a result, the QBO period and amplitude in GLENS remain mostly unchanged relative to present day with slightly more Easterlies, reflected as a negative zonal mean wind anomaly. The power spectrum of the QBO under GEQ is relatively flat, showing no well-defined oscillation. The QBO spectrum shown in Figure 15 is calculated at ≈30 hPa, where there is no obvious oscillation; there is no obvious cycle at ≈20 hPa either (not shown). However, the height of the oscillation in the GEQ simulation appears to move vertically (Figure 15), whereas the QBO in the other simulations tends to remain at a relatively constant altitude, so the flat spectrum may be due to difficulty in selecting an appropriate altitude for computation of the QBO index in the GEQ simulation.

## 5. Conclusions

A comparison of the two geoengineering ensembles explored here shows that while both GLENS and GEQ are effective at offsetting global mean temperature changes, GLENS (with multiple injection locations) is more effective at offsetting changes in the equator-to-pole temperature gradient. In addition, regional residual temperature effects (which were not chosen as explicit objectives in either ensemble) are lower in GLENS than GEQ, as are other changes in surface climate such as precipitation and sea ice coverage, all with lower total injection amounts than in GEQ. As such, the motivation behind including multiple simultaneous objectives has been demonstrated to be well founded: including more objectives can yield improved control over more aspects of the climate system. As has been discussed by Kravitz et al. (2017) among others, we do not yet understand the boundaries of achievable climate objectives (MacMartin & Kravitz, 2019b). However, the results presented here regarding GEQ echo previous studies of geoengineering using solar reduction: offsetting changes in $T_0$ also offsets many other climatic changes (Govindasamy & Caldeira, 2000; Kravitz et al., 2013; Kravitz et al., 2016).

In addition, the stratospheric effects presented here for GEQ are similar to what others have seen: despite achieving a negative radiative forcing in most regions of the globe, the spatial distribution of the aerosols
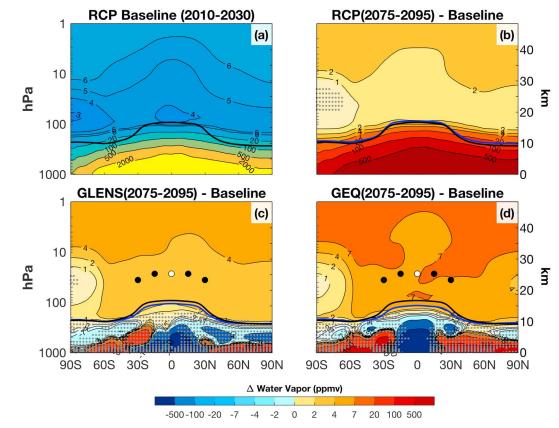
**Figure 13.** As in Figure 10 but for water vapor (ppm$_v$).

tends to peak in the tropics, resulting in larger particles, consequent stratospheric heating, increased stratospheric water vapor, a persistent Westerly phase of the QBO, and surface temperature changes that could be associated with dynamical effects. However, the comparisons undertaken here also indicate that off-GEQ, such as in GLENS, ameliorates some of these effects. It is particularly instructive that although tropical injection was originally proposed for efficiency to let atmospheric transport do a lot of the "work" of deployment, the simulations discussed here show that in the model employed here, there is at least one off-GEQ strategy that is more efficient than GEQ.

Despite some similarities between the results presented here and those in other studies, there are notable differences among some aspects. Examples include transport of aerosols out of the tropics (Niemeier & Timmreck, 2015) and the radiation code (Kleinschmitt et al., 2018), which results in different fluxes and forcing efficiency. Niemeier and Tilmes (2017) provide an estimate of uncertainty in the forcing efficiency of stratospheric sulfate aerosol injection. Although other results presented here are consistent with their results, the uncertainty is so large (up to a factor of ~6 for the highest injection rates they investigated) that our study does not provide any additional constraints on this issue. Further work, including model intercomparison with equatorial and GLENS-like setups, and in particular setups that can control for stratospheric heating, will be necessary to properly quantify forcing efficiency which, ultimately, determines how much injection is needed to achieve particular climate effects.

The "efficiency improvement" in temperature reduction of 19% in GLENS as compared to GEQ has important implications for potential nonlinearities. Although the injection rates explored here did not venture into a highly nonlinear regime, in general, less perturbation is less likely to excite or exacerbate nonlinear behavior (MacMartin et al., 2016), which better retains predictability and which makes employment of a feedback algorithm more likely to succeed (MacMartin et al., 2014; Kravitz et al., 2014). As was shown in Figure 3, the relationship between injection rate and stratospheric AOD is consistent between the two ensembles. AOD is a function of mass loading and particle size. From Figures 10 and 11, GLENS has less mass loading than GEQ and also a smaller effective radius in general. However, effective radius in GLENS grows throughout
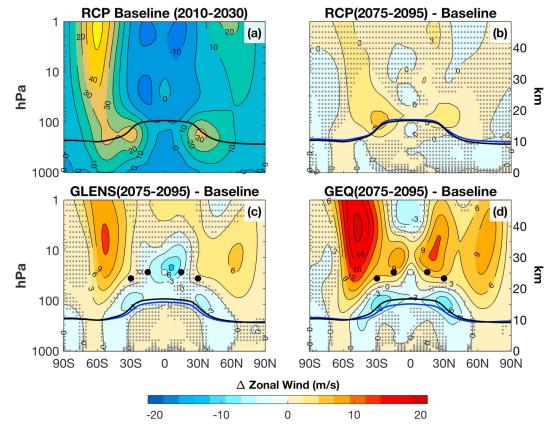
**Figure 14.** As in Figure 10 but for zonal wind (m/s). Positive values in panel (a) indicate Westerly flow.

the simulation (also, see Figure S6). As such, it is plausible that there would be a consistent relationship between injection rate and AOD, and the increased cooling efficiency in GLENS is due to its ability to maintain lower injection rates to meet the same objective (here, $T_0$), not directly in its ability to prevent large particle growth. We acknowledge the potential for resolution dependence of any linear/nonlinear behavior, in that subgrid behavior of the particles may not adequately reproduce what might happen in real-world deployment.

Although GLENS did not fully meet the $T_2$ objective, Kravitz et al. (2017) demonstrated that the $T_2$ objective was fully met via the same feedback algorithm in an earlier version of CESM1(WACCM), without encountering a situation in which meeting the objectives would have required negative injection at a location. As of yet, we are uncertain as to the cause of this discrepancy, but we hypothesize it is due to a change in land models between the two versions. While the exact source of this difference still needs to be investigated, it raises an important point regarding behavior of the feedback algorithm in the presence of uncertainty. Structural uncertainties surrounding the land model used here could have led to notably different performance in meeting the objectives for the same feedback algorithm. Should this strategy be employed in future studies, care will need to be taken to further reduce uncertainties and to improve feedback algorithm robustness. It would also be worthwhile to understand the broader range of processes involved in responses to geoengineering. Possible simulations could include conducting these same experiments in slab-ocean, atmosphere-only, or aquaplanet contexts.

These two ensembles are by far not the only plausible representations of geoengineering in modeling studies. Different objectives may require different geoengineering strategies, and it seems likely that some uncertainties will be irreducible, necessitating strategies to manage uncertainties. The present study was, in effect, a demonstration that applying feedback to meet multiple objectives can, under certain metrics, outperform more naive strategies of geoengineering. Advancing this research could follow a more thorough, systematic effort to ensure that research needs are prioritized and the most important uncertainties are being addressed (MacMartin & Kravitz, 2019a).
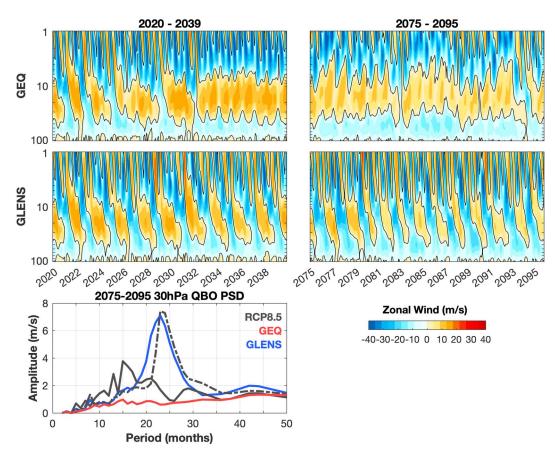
**Figure 15.** Changes in the QBO under equatorial injection (top row) and GLENS (middle row). Top and middle rows show zonal mean zonal wind, averaged over 2°S to 2°N, over the periods 2020–2039 and 2075–2095. Positive values indicate Westerly flow. Bottom panel shows power spectra of the QBO, indicating period and amplitude. Baseline values in the bottom panel are represented by the dashed line. QBO = quasi-biennial oscillation; RCP = Representative Concentration Pathway; GLENS = Geoengineering Large Ensemble; GEQ = equatorial injection.

## References

Aquila, V., Garfinkel, C. I., Newman, P. A., Oman, L. D., & Waugh, D. W. (2014). Modifications of the quasi-biennial oscillation by a geoengineering perturbation of the stratospheric aerosol layer. *Geophysical Research Letters*, *41*, 1738–1744.

Bala, G., Duffy, P. B., & Taylor, K. E. (2008). Impact of geoengineering schemes on the global hydrological cycle. *Proceedings of the National Academy of Sciences*, *105*, 7664–7669.

Ban-Weiss, G. A., & Caldeira, K. (2010). Geoengineering as an optimization problem. *Environmental Research Letters*, *5*, 031001.

Budyko, M. I. (1977). *Climatic changes*. American Geophysical Union.

Caldeira, Ken, Bala, G., & Cao, L. (2013). The science of geoengineering. *Annual Review of Earth and Planetary Sciences*, *41*, 231–256.

Crutzen, P. J. (2006). Albedo enhancement by stratospheric sulfur injections: A contribution to resolve a policy dilemma? *Climatic Change*, *77*, 211–220.

Dai, Z., Weisenstein, D. K., & Keith, D. W. (2018). Tailoring meridional and seasonal radiative forcing by sulfate aerosol solar geoengineering. *Geophysical Research Letters*, *45*, 1030–1039.

Danabasoglu, G., Bates, S., Briegleb, B., Jayne, S., Jochum, M., Large, W., et al. (2012). The CCSM4 ocean component. *Journal of Climate*, *25*, 1361–1389. https://doi.org/10.1175/JCLI-D-11-00091.1

Driscoll, S., Bozzo, A., Gray, L. J., Robock, A., & Stenchikov, G. (2012). Coupled Model Intercomparison Project 5 (CMIP5) simulations of climate following volcanic eruptions. *Journal of Geophysical Research*, *117*, D17105.

English, J. M., Toon, O. B., & Mills, M. J. (2012). Microphysical simulations of sulfur burdens from stratospheric sulfur geoengineering. *Atmospheric Chemistry and Physics*, *12*, 4775–4793.

Frierson, D. M. W., & Hwang, Y.-T. (2012). Extratropical influence on ITCZ shifts in slab ocean simulations of global warming. *Journal of Climate*, *25*, 720–733.

Govindasamy, B., & Caldeira, K. (2000). Geoengineering Earth's radiation balance to mitigate $CO_2$-induced climate change. *Geophysical Research Letters*, *27*, 2141–2144.

Hansen, J. E., Sato, M., Ruedy, R., Nazarenko, L., Lacis, A., Schmidt, G. A., et al. (2005). Efficacy of climate forcings. *Journal of Geophysical Research*, *110*, D18104.

Heckendorn, P., Weisenstein, D., Fueglistaler, S., Luo, B. P., Rozanov, E., Schraner, M., et al. (2009). The impact of geoengineering aerosols on stratospheric temperature and ozone. *Environmental Research Letters*, *4*, 045108.

Holland, M. M., & Bitz, C. M. (2003). Polar amplification of climate change in coupled models. *Climate Dynamics*, *21*, 221–232.

Hunke, E. C., & Lipscomb, W. H. (2008). CICE: The Los Alamos sea ice model: Documentation and software user's manual, version 4.0 (Tech. Rep. LA-CC-06-012): T-3 Fluid Dynamics Group, Los Alamos National Laboratory.

Hwang, Y.-T., & Frierson, D. M. W. (2010). Increasing atmospheric poleward energy transport with global warming. *Geophysical Research Letters*, *37*, L24807. https://doi.org/10.1029/2010GL045440

Irvine, P. J., Kravitz, B., Lawrence, M. G., & Muri, H. (2016). An overview of the Earth system science of solar geoengineering. *WIREs Climate Change*, *7*, 815–833.

Kleinschmitt, C., Boucher, O., & Platt, U. (2018). Sensitivity of the radiative forcing by stratospheric sulfur geoengineering to the amount and strategy of the $SO_2$ injection studied with the LMDZ-S3A model. *Atmospheric Chemistry and Physics*, *18*, 2769–2786.

Kravitz, B., Caldeira, K., Boucher, O., Robock, A., Rasch, P. J., Alterskjær, K., et al. (2013). Climate model response from the Geoengineering Model Intercomparison Project (GeoMIP). *Journal of Geophysical Research: Atmospheres*, *118*, 8320–8332.

Kravitz, B., MacMartin, D. G., Leedal, D. T., Rasch, P. J., & Jarvis, A. J. (2014). Explicit feedback and the management of uncertainty in meeting climate objectives with solar geoengineering. *Environmental Research Letters*, *9*, 044006.

Kravitz, B., MacMartin, D. G., Mills, M. J., Richter, J. H., Tilmes, S., Lamarque, J. F., et al. (2017). First simulations of designing stratospheric sulfate aerosol geoengineering to meet multiple simultaneous climate objectives. *Journal of Geophysical Research: Atmospheres*, *122*, 12,616–12,634.

Kravitz, B., MacMartin, D. G., Wang, H., & Rasch, P. J. (2016). Geoengineering as a design problem. *Earth System Dynamics*, *7*, 469–497.

Kravitz, B., & Robock, A. (2011). Climate effects of high-latitude volcanic eruptions: Role of the time of year. *Journal of Geophysical Research*, *116*, D01105.

Kravitz, B., Robock, A., Oman, L., Stenchikov, G., & Marquardt, A. B. (2009). Sulfuric acid deposition from stratospheric geoengineering with sulfate aerosols. *Journal of Geophysical Research*, *114*, D14109.

Liu, X., Easter, R. C., Ghan, S. J., Zaveri, R. A., Rasch, P. J., Shi, X., et al. (2012). Toward a minimal representation of aerosols in climate models: Description and evaluation in the Community Atmosphere Model CAM5. *Geoscientific Model Development*, *5*, 709–739. https://doi.org/10.5194/gmd-5-709-2012

MacMartin, D. G., Douglas G., Kravitz, B., Tilmes, S., Richter, J. H., Mills, M. J., et al. (2017). The climate response to stratospheric aerosol geoengineering can be tailored using multiple injection locations. *Journal of Geophysical Research: Atmospheres*, *122*, 12,574–12,590.

MacMartin, D. G., & Kravitz, B. (2019a). Mission-driven research for stratospheric aerosol geoengineering. *Proceedings of the National Academy of Sciences of the United States of America*, *116*, 1089–1094.

MacMartin, D. G., & Kravitz, B. (2019b). The engineering of climate engineering. *Annual Reviews Control Robotics Autonomous Systems*, *2*, 1–23.

MacMartin, D. G., Kravitz, B., Keith, D. W., & Jarvis, A. (2014). Dynamics of the coupled human-climate system resulting from closed-loop control of solar geoengineering. *Climate Dynamics*, *43*, 243–258.

MacMartin, D. G., Kravitz, B., Long, J. C. S., & Rasch, P. J. (2016). Geoengineering with stratospheric aerosols: What don't we know after a decade of research? *Earth's Future*, *4*, 543–548.

MacMartin, D. G., Wang, W., Kravitz, B., Tilmes, S., Richter, J., & Mills, M. J. (2019). Timescale for detecting the climate response to stratospheric aerosol geoengineering. *Journal of Geophysical Research: Atmospheres*, *124*, 1233–1247.

Manabe, S., & Wetherald, R. T. (1975). The effects of doubling the $CO_2$ concentration on the climate of a general circulation model. *Journal of the Atmospheric Sciences*, *32*, 3–15.

Mills, M. J., Richter, JadwigaH., Tilmes, S., Kravitz, B., MacMartin, D. G., Glanville, A. A., et al. (2017). Radiative and chemical response to interactive stratospheric sulfate aerosols in fully coupled CESM1(WACCM). *Journal of Geophysical Research: Atmospheres*, *122*, 13,061–13,078.

NRC (2015). Climate intervention: Reflecting sunlight to cool Earth: National Research Council. (last access: 7 May 2015).

Niemeier, U., & Schmidt, H. (2017). Changing transport processes in the stratosphere by radiative heating of sulfate aerosols. *Atmospheric Chemistry and Physics*, *17*, 14,871–14,886.

Niemeier, U., Schmidt, H., & Timmreck, C. (2011). The dependency of geoengineered sulfate aerosol on the emission strategy. *Atmospheric Chemistry and Physics*, *12*, 189–194.

Niemeier, U., & Tilmes, S. (2017). Sulfur injections for a cooler planet. *Science*, *357*, 246–248.

Niemeier, U., & Timmreck, C. (2015). What is the limit of climate engineering by stratospheric injection of $SO_2$? *Atmospheric Chemistry and Physics*, *15*, 9129–9141.

Oleson, K., et al. (2013). Technical description of version 4.5 of the Community Land Model (CLM) (10.5065/D6RR1W7M, technical Note NCAR/TN-503+STR). National Center for Atmospheric Research.

Oman, L., & Waugh, D. W. (2008). Understanding the changes of stratospheric water vapor in coupled chemistry-climate model simulations. *Journal of the Atmospheric Sciences*, *65*, 3278–3291. https://doi.org/10.1175/2008JAS2696.1.

Pierce, J. R., Weisenstein, D. K., Heckendorn, P., Peter, T., & Keith, D. W. (2010). Efficient formation of stratospheric aerosol for climate engineering by emission of condensible vapor from aircraft. *Geophysical Research Letters*, *37*, L18805.

Pitari, G., Aquila, V., Kravitz, B., Robock, A., Watanabe, S., Luca, N. D., et al. (2014). Stratospheric ozone response to sulfate geoengineering: Results from the Geoengineering Model Intercomparison Project (GeoMIP). *Journal of Geophysical Research: Atmospheres*, *119*, 2629–2653.

Plumb, R. A. (2002). Stratospheric transport. *Journal of the Meteorological Society of Japan*, *80*, 793–809.

Rasch, P. J., Tilmes, S., Turco, R. P., Robock, A., Oman, L., Chen, C., et al. (2008b). An overview of geoengineering of climate using stratospheric sulphate aerosols. *Philosophical Transactions of the Royal Society A*, *366*, 4007–4037.

Richter, J. H., S. Tilmes, Glanville, A., Kravitz, B., MacMartin, D. G., Mills, M. J., et al. (2018). Stratospheric response in the first geoengineering simulation meeting multiple surface climate objectives. *Journal of Geophysical Research: Atmospheres*, *123*, 5762–5782.

Richter, J. H., Tilmes, S., Mills, M. J., Tribbia, J. J., Kravitz, B., MacMartin, D. G., et al. (2017). Stratospheric dynamical response and ozone feedbacks in the presence of $SO_2$ injections. *Journal of Geophysical Research: Atmospheres*, *122*, 12,557–12,573.

Robock, A. (2000). Volcanic eruptions and climate. *Reviews of Geophysics*, *38*, 191–219.

Robock, A., & Mao, J. (1992). Winter warming from large volcanic eruptions. *Geophysical Research Letters*, *19*, 2405–2408.

Robock, A., Oman, L., & Stenchikov, G. L. (2008). Regional climate responses to geoengineering with tropical and Arctic $SO_2$ injections. *Journal of Geophysical Research*, *113*, D16101.

Tilmes, S., Garcia, R. R., Kinnison, D. E., Gettelman, A., & Rasch, P. J. (2009). Impact of geoengineered aerosols on the troposphere and stratosphere. *Journal of Geophysical Research*, *114*, D12305.

Tilmes, S., J. H. Richter, Kravitz, B., MacMartin, D. G., Mills, M. J., Simpson, I., et al. (2018). CESM1(WACCM) Stratospheric Aerosol Geoengineering Large Ensemble project. *Bulletin of the American Meteorological Society*, *99*, 2361–2371. https://doi.org/10.1175/BAMS-D-17-0267.1

Tilmes, S., Müller, R., & Salawitch, R. (2008). The sensitivity of polar ozone depletion to proposed geoengineering schemes. *Science*, *320*, 120–1204.

Tilmes, S., Richter, J. H., Mills, M. J., Kravitz, B., MacMartin, D. G., Garcia, R. R., et al. (2018). Effects of different stratospheric $SO_2$ injection altitudes on stratospheric chemistry and dynamics. *Journal of Geophysical Research: Atmospheres*, *123*, 4654–4673.

Tilmes, S., Richter, J. H., Mills, M. J., MacMartin, D. G., Vitt, F., Tribbia, J. J., et al. (2017). Sensitivity of aerosol distribution and climate response to stratospheric $SO_2$ injection locations. *Journal of Geophysical Research: Atmospheres*, *122*, 12,591–12,615.

van Vuuren, D. P., Edmonds, J., Kainuma, M., Riahi, K., Thomson, A., Hibbard, K., et al. (2011). The representative concentration pathways: An overview. *Climatic Change*, *109*, 5.

Vattioni, S., Weisenstein, D., Keith, D., Feinberg, A., Peter, T., & Stenke, A. (2019). Exploring accumulation-mode-$H_2$ $SO_4$ versus $SO_2$ stratospheric sulfate geoengineering in a sectional aerosol-chemistry-climate model. *Atmospheric Chemistry and Physics*, *19*, 4877–4897. https://doi.org/10.5194/acp-19-4877-2019

Visioni, D., Pitari, G., Tuccella, P., & Curci, G. (2018). Sulfur deposition changes under sulfate geoengineering conditions: quasi-biennial oscillation effects on the transport and lifetime of stratospheric aerosols. *Atmospheric Chemistry and Physics*, *18*, 2787–2808.

Wunderlich, F., & Mitchell, D. M. (2017). Revisiting the observed surface climate response to large volcanic eruptions. *Atmospheric Chemistry and Physics*, *17*, 485–499.

Wunsch, C. (2005). The total meridional heat flux and its oceanic and atmospheric partition. *Journal of Climate*, *18*, 4374–4380.